

Orbital-driven Mottness collapse in 1T-TaS_{2-x}Se_x transition metal dichalcogenide

Shuang Qiao^{1,2,*}, Xintong Li^{1,*}, Naizhou Wang³, Wei Ruan¹, Cun Ye¹, Peng Cai¹, Zhenqi Hao¹,
Hong Yao^{2,4}, Xianhui Chen^{3,5}, Jian Wu^{1,4,†}, Yayu Wang^{1,4,†}, Zheng Liu^{2,4,†}

¹*State Key Laboratory of Low Dimensional Quantum Physics, Department of Physics, Tsinghua University, Beijing 100084, P.R. China*

²*Institute for Advanced Study, Tsinghua University, Beijing 100084, P.R. China*

³*Hefei National Laboratory for Physical Science at Microscale and Department of Physics, University of Science and Technology of China, Hefei, Anhui 230026, P.R. China*

⁴*Innovation Center of Quantum Matter, Beijing 100084, P.R. China*

⁵*Collaborative Innovation Center of Advanced Microstructures, Nanjing University, Nanjing 210093, China*

*These authors contributed equally to this work.

†Email: wu@phys.tsinghua.edu.cn; yayuwang@tsinghua.edu.cn; zliu@phys.tsinghua.edu.cn

The vicinity of a Mott insulating phase has constantly been a fertile ground for finding exotic quantum states, most notably the high T_c cuprates and colossal magnetoresistance manganites. The layered transition metal dichalcogenide 1T-TaS₂ represents another intriguing example, in which the Mott insulator phase is intimately entangled with a series of complex charge-density-wave (CDW) orders. More interestingly, it has been recently found that 1T-TaS₂ undergoes a Mott-insulator-to-superconductor transition induced by high pressure, charge doping, or isovalent substitution. The nature of the Mott insulator phase and transition mechanism to the conducting state is still under heated debate. Here, by combining scanning tunneling microscopy (STM) measurements and first-principles calculations, we investigate the atomic scale electronic structure of 1T-TaS₂ Mott insulator and its evolution to the metallic state upon isovalent substitution of S with Se. We identify two distinct types of orbital textures - one localized and the other extended - and demonstrates that the interplay between them is the key factor that determines the electronic structure. Especially, we show that the continuous evolution of the charge gap visualized by STM is due to the immersion of the localized-orbital-induced Hubbard bands into the extended-orbital-spanned Fermi sea, featuring a unique evolution from a Mott gap to a charge-transfer gap. This new mechanism of orbital-driven Mottness collapse revealed here suggests an interesting route for creating novel electronic state and designing future electronic devices.

1T-TaS₂ has a trilayered (TL) structure as shown in Fig. 1a, in which the Ta atoms form a planar triangular lattice sandwiched by two S-atom planes. It exhibits a series of complex CDW orders at various temperature (T) ranges, including an incommensurate CDW at high T , a nearly commensurate CDW (NCCDW) at intermediate T , and a commensurate CDW (CCDW) order in

the ground state¹⁻³. The Mott insulator phase is believed to be a consequence of the CCDW order³⁻⁷. Superconductivity emerges as the Mott insulator state is suppressed by pressure or doping⁸⁻¹⁵, and the electronic phase diagram^{9,11,13,15} displays many similarities to that of the cuprates. Currently there are many debates about the nature of the Mott insulator and how it evolves into the metallic and eventually superconducting state^{9,10,12,14,16-22}. Much of the challenge originates from the observation that the electronic structure may be influenced by a number of factors, including the CDW superstructure, phase separation and domain boundaries, strong disorders, spin-orbit coupling and interlayer coupling.

STM is an ideal experimental technique for probing the atomic scale electronic structure of complex materials. Figure 1b displays the STM topographic image of pristine 1T-TaS₂, which clearly reveals the CCDW order with a $\sqrt{13} \times \sqrt{13}$ superlattice where 13 Ta atoms form a Star-of-David (SD) structure. Note that the bright spots correspond to the S atoms lying in the uppermost layer, and the position of the Ta atoms can be determined according to the octahedral coordination. In Fig. 1c we show the spatially averaged differential conductance (dI/dV), which is approximately proportional to the electron density of states (DOS), of pristine 1T-TaS₂. An energy gap around the Fermi level (E_F) can be clearly observed, which is attributed to the Mott-Hubbard gap of the insulating CCDW phase.

These spectroscopic features can be captured by density functional theory (DFT) calculations including the onsite Hubbard U correction in a Hartree-Fock manner²³. Figure 1d shows the obtained band structure of a 1T-TaS₂ TL with the CCDW superstructure. There is a full charge gap around the E_F , which is bounded by two narrow bands, corresponding to the upper and lower Hubbard bands, respectively. The gap size is found to depend on the Hubbard repulsion U and a choice of $U = 2.27$ eV as previously derived from the linear-response calculation is used to

reproduce the experimental value²³. By turning off the $+U$ correction and the spin degree of freedom, in a plain DFT calculation the charge gap will collapse and the two narrow bands become degenerate, giving a half-filled metallic state (Supplementary Fig. S4). These results corroborate a Mott origin of the charge gap. There is another energy gap below the lower Hubbard band isolating it from the underneath dispersive band continuum (shaded in blue in Fig. 1d), which is commonly referred to as the CDW gap (Δ_{CDW})²⁴⁻²⁶. This gap is manifested in the dI/dV spectrum as a dip below the lower Hubbard peak (Fig. 1c).

Besides the CCDW superstructure and energy spectrum, equally important is the local DOS (LDOS) mapping at selected energies, which contains the spatial characteristics of electronic wavefunctions, i.e., the orbital texture. Figure 2a displays the dI/dV , or LDOS, mapping measured at two representative energies. At $V_b = -207$ mV (upper panel), which corresponds to the lower Hubbard band, the LDOS map shows a periodic pattern that is commensurate with the CCDW superlattice. By comparing the LDOS map with the topographic image of the same area (Fig. 1b), the bright spots are identified to be the center of SDs. Moving to lower energy with bias $V_b = -422$ mV (lower panel), a distinctly different orbital texture is revealed: the LDOS map exhibits a kagome-like superstructure. Its bright/dark spots are inverse of the previous texture, indicating contributions mainly from the surrounding Ta orbitals. LDOS maps at positive biases give a nearly symmetric picture: the upper Hubbard band corresponds to an orbital texture concentrated on the center of SDs, whereas at higher energy the bright spots shift to the surrounding Ta orbitals (Supplementary Fig. S2).

To determine the nature of these two orbital textures discussed above, we proceed by performing *ab initio* Wannier function analysis²⁷⁻²⁹. In the plain DFT band structure, the 6

dispersive bands below E_F and the narrow bands near E_F represent a seven-orbital subspace, which will accommodate the thirteen unpaired d -electrons in a SD. Within this subspace, the spatial distributions of the seven Wannier functions are plotted in Fig. 2b, which automatically separate into two groups. The one denoted by $|c\rangle$ concentrates at the central Ta atom with a typical d_{z^2} geometry. The remaining six Wannier functions distribute dominantly along the edge of the SD ($|s_{\alpha=1\dots 6}\rangle$), which can be viewed as the bonding orbitals of the surrounding Ta atoms. The reconstructed band structure using $|c\rangle$ and $|s_{\alpha=1\dots 6}\rangle$ as basis well reproduces the DFT result (Supplementary Fig. S4). This Wannier function analysis gives a natural explanation for the two types of orbital textures observed by STM. In particular, it clarifies that the kagome-like texture arises from a set of linear-shaped molecular orbitals.

At first glance, the orbital texture below Δ_{CDW} , i.e. $|s_{\alpha=1\dots 6}\rangle$, appears to be irrelevant to the low-energy physics. Indeed, in previous studies the electronic evolution is generally discussed based on a one-band Hubbard model employing the $|c\rangle$ orbital alone^{20,30,31}. Since this orbital is largely localized, it is susceptible to a Mott transition, giving rise to the upper and lower Hubbard bands. However, it is important to note that the validity of the one-band Hubbard model is protected by a large Δ_{CDW} . When the CCDW order is weakened, a one-band-to-multi-band transition has to be considered, which in turn plays an important role in the collapse of the Mott phase.

To test the validity of the two-orbital model, we further investigate the electronic structure of 1T-TaS₂ under external influence. A rather gentle perturbation to the 1T-TaS₂ structure is to modify the buckling of the S atoms around the central Ta, which is expected to affect the CCDW order. Experimentally this can be effectively realized through isovalent substitution of S by Se^{12,13},

which has a larger ionic size and thus increases the buckling of the surrounding S atoms. We have synthesized a series of Se-doped 1T-TaS₂ single crystals, whose transport properties are shown in Supplementary Fig. S1. Figure 3a displays a large area STM image on the surface of a sample with Se content $x = 0.5$. Unlike the pristine sample (Fig. 1b), the surface structure now splits into domains with varied domain size and sharp boundaries in between (Fig. 3a), which resembles the so-called “mosaic” phase in 1T-TaS₂ induced by voltage pulse in STM experiments^{32,33}. A closer examination around the domain walls reveals both translational and 30° degree rotational mismatch between different domains (Supplementary Fig. S3). Increasing the Se concentration from $x = 0.5$ to $x = 1$ creates more domain walls and defects, but the general topographic properties remain the same. As shown in Fig. 3b, within a single domain the CCDW superlattice retains the SD patterns as that in the undoped TaS₂ sample. Atomic-precision topography shows intensity modulation of the pristine lattice periodicity, suggesting spatial inhomogeneity of Se concentration.

Figure 3c shows the dI/dV spectra measured at various locations on the surface of the $x = 1$ sample, which exhibit a continuous evolution. There are still small areas showing a spectrum similar to that in pristine 1T-TaS₂ with a nearly unperturbed Mott gap (black curve), indicating very low concentration of Se dopants locally. Moving upwards, the Mottness gap shrinks continuously, presumably due to increasing Se doping (red and blue curves). With further shrinking of the Mott gap, a broad V-shaped gap forms near E_F , which looks reminiscent of the pseudogap in underdoped cuprates. The V-shaped gap also shrinks gradually, and a finite DOS appears at E_F , indicating the transition into a metallic state. Eventually the gap vanishes completely and a sharp peak emerges near E_F , which looks similar to the Van Hove singularity (VHS) in overdoped cuprates. There is a clear collapse of the Mottness gap induced by Se substitution of S, which underlies the Mott insulator to metal phase transition.

To simulate the STM results on Se-doped 1T-TaS₂, we performed DFT+U calculations on supercells with different Se concentration. For a given Se concentration, the lowest-energy substitution configuration is determined, and the DFT structural relaxation confirms that the main effect of Se substitution is to increase the local buckling of the TL. The evolution of the band structure is traced in Fig. 4, which reveals the complete Mott-insulator-to-metal transition process. At low-doping concentration, despite a reduction of Δ_{CDW} , E_g stays unchanged as it is dictated by the effective Hubbard U of the $|c\rangle$ -orbital alone. After the lower Hubbard band touches the $|s_\alpha\rangle$ -orbital bands, the Mott gap transforms into the charge-transfer type gap because now the lowest energy excitation is from the continuum band formed by the $|s_\alpha\rangle$ -orbitals to the upper Hubbard band formed by the $|c\rangle$ -orbital. The gap size shrinks continuously upon further doping. According to the calculation, the critical point is reached at $x \approx 0.92$, where the indirect charge-transfer gap becomes zero. Beyond this critical doping concentration, the upper Hubbard band also sinks into the $|s_\alpha\rangle$ -orbital bands, driving the system into the metallic regime. For the high-doping case, the $|c\rangle$ -orbital and $|s_\alpha\rangle$ -orbitals are strongly hybridized so that we can barely see the remnants of the narrow upper Hubbard band around the Γ point at E_F . We plot the DOS evolution as a function of Se concentration in Fig. 3d, rendering a direct comparison with the STM dI/dV spectra of 1T-TaS_{2-x}Se_x samples. The U-shaped Motttness gap, the V-shaped pseudogap, and the sharp VHS-type peak are all nicely reproduced in the theoretical simulation. The excellent agreement between theory and experiment confirms the validity of the orbital-driven Mott insulator to metal transition.

We note that in the calculation no additional complexities, such as spin-orbit coupling, inter-TL coupling and disorder, are introduced. We believe that the interplay between the $|c\rangle$ -orbital and $|s_\alpha\rangle$ -orbitals represents a universal origin of Motttness collapse in 1T-TaS₂, no matter via

mechanical or chemical routes. To capture the essential physics of such novel Mottness collapse, we propose a generalized effective multi-orbital Hubbard model as formulated below:

$$H = \Delta_{SD} \sum_I c_I^\dagger c_I + t_{cs} \sum_{I\alpha} (c_I^\dagger s_{I\alpha} + H. c.) + \sum_{I\alpha, J\beta} t_{ss}^{I\alpha, J\beta} s_{I\alpha}^\dagger s_{J\beta} + U \sum_I c_{I\uparrow}^\dagger c_{I\downarrow}^\dagger c_{I\downarrow} c_{I\uparrow}, \quad (1)$$

Where Δ_{SD} is the onsite energy difference between $|c\rangle$ and $|s_{\alpha=1\dots 6}\rangle$ generated by the formation of SD (Fig. 4b), and I, J indexes the SDs. The central orbital $|c\rangle$ experiences an onsite Coulomb repulsion U , whereas the interaction terms of $|s_{\alpha=1\dots 6}\rangle$ are neglected considering they are less localized. The values of Δ_{SD} and the dominant hopping parameter (t) can be extracted by exploiting the same Fourier transformation as used in the Wannier function analysis. We list the key parameters for three typical 1T-TaS₂ samples in the Supplementary Tab. SI.

According to this effective model, we schematically summarize the overall physics of the orbital-driven electronic structure evolution in Se doped 1T-TaS₂ (Fig. 4b). The key ingredient is the organization of the two types of orbital textures $|c\rangle$ and $|s_{\alpha=1\dots 6}\rangle$ accompanied by the formation of the SD structures (Fig. 2). The central orbital is isolated by the surrounding ones, making inter-cluster hopping of central-orbital electrons possible only via high-order process. It is thus susceptible to a Mott transition when $|c\rangle$ is separated from $|s_{\alpha}\rangle$ in energy (left panel of Fig. 4). On the other hand, the $|s_{\alpha}\rangle$ orbitals are extended with sizable hopping amplitude, naturally giving rise to a metallic phase when $|c\rangle$ and $|s_{\alpha}\rangle$ mix (right panel of Fig. 4). For the large Δ_{SD} limit, this model can be reduced to the one-band Hubbard model by integrating out the $|s_{\alpha}\rangle$ orbitals. However, the single-orbital half-filling condition no longer holds when Δ_{SD} becomes small, which can be achieved by either structural perturbation or chemical doping.

Our experimental observations and first-principle calculations in 1T-TaS₂ reveal a new mechanism of Mottness collapse, which is fundamentally different from previously known examples such as charge-doping-induced collapse in cuprates and pressure-induced collapse in weak Mott insulators. In the layered 1T-TaS₂, the isovalent substitution of S with Se does not induce additional charge carriers. Instead, it tunes the CDW order, and in turn drives the direct Mott gap into an effective “charge-transfer” gap. To the best of our knowledge, it is the first time that such a novel evolution between Mott gap and charge-transfer gap can be adiabatically accessed in the same material. Upon further substitution, after the charge gap fully collapses, the low energy degrees of freedom include the Fermi-surface-forming itinerant carriers and fluctuating local magnetic moments, from which the superconductivity emerges, just like in heavy-fermion superconductors and iron-based superconductors. It is thus interesting to ask whether this parent state for superconductivity is a heavy fermion liquid or a magnetic metal. We believe that the richness of the orbital-tunable electronic structure in Se-doped TaS₂ will shed important insights into several important topics of modern condensed matter physics.

References

- 1 Wilson, J. A., Di Salvo, F. J. & Mahajan, S. Charge-density waves and superlattices in the metallic layered transition metal dichalcogenides. *Advances in Physics* **24**, 117-201 (1975).
- 2 Scruby, C. B., Williams, P. M. & Parry, G. S. The role of charge density waves in structural transformations of 1T-TaS₂. *Philosophical Magazine* **31**, 255-274 (1975).
- 3 Fazekas, P. & Tosatti, E. Electrical, structural and magnetic properties of pure and doped 1T-TaS₂. *Philosophical Magazine Part B* **39**, 229-244 (1979).
- 4 Fazekas, P. & Tosatti, E. Charge carrier localization in pure and doped 1T-TaS₂. *Physica B+C* **99**, 183 (1980).
- 5 Dardel, B. *et al.* Temperature-dependent pseudogap and electron localization in 1T-TaS₂. *Physical Review B* **45**, 1462-1465 (1992).

- 6 Dardel, B. *et al.* Spectroscopic signatures of phase transitions in a charge-density-wave system: 1T-TaS₂. *Physical Review B* **46**, 7407-7412 (1992).
- 7 Kim, J. J., Yamaguchi, W., Hasegawa, T. & Kitazawa, K. Observation of Mott localization gap using low temperature scanning tunneling spectroscopy in commensurate 1T-TaS₂. *Physical review letters* **73**, 2103-2106 (1994).
- 8 Morosan, E. *et al.* Superconductivity in Cu_xTiSe₂. *Nature Physics* **2**, 544-550 (2006).
- 9 Sipos, B. *et al.* From Mott state to superconductivity in 1T-TaS₂. *Nature Materials* **7**, 960-965 (2008).
- 10 Ang, R. *et al.* Real-space coexistence of the melted Mott state and superconductivity in Fe-substituted 1T-TaS₂. *Physical review letters* **109**, 176403 (2012).
- 11 Li, L. J. *et al.* Fe-doping-induced superconductivity in the charge-density-wave system 1T-TaS₂. *EPL (Europhysics Letters)* **97**, 67005 (2012).
- 12 Ang, R. *et al.* Superconductivity and bandwidth-controlled Mott metal-insulator transition in 1T-TaS_{2-x}Se_x. *Physical Review B* **88**, 115145 (2013).
- 13 Liu, Y. *et al.* Superconductivity induced by Se-doping in layered charge-density-wave system 1T-TaS_{2-x}Se_x. *Applied Physics Letters* **102**, 192602 (2013).
- 14 Ang, R. *et al.* Atomistic origin of an ordered superstructure induced superconductivity in layered chalcogenides. *Nature Communications* **6**, 6091 (2015).
- 15 Yu, Y. *et al.* Gate-tunable phase transitions in thin flakes of 1T-TaS₂. *Nature Nanotechnology* **10**, 270-276 (2015).
- 16 Mutka, H., Zuppiroli, L., Molinié, P. & Bourgoïn, J. C. Charge-density waves and localization in electron-irradiated 1T-TaS₂. *Physical Review B* **23**, 5030-5037 (1981).
- 17 Bovet, M. *et al.* Interplane coupling in the quasi-two-dimensional 1T-TaS₂. *Physical Review B* **67**, 125105 (2003).
- 18 Rossnagel, K. & Smith, N. V. Spin-orbit coupling in the band structure of reconstructed 1T-TaS₂. *Physical Review B* **73**, 0731066 (2006).
- 19 Xu, P. *et al.* Superconducting phase in the layered dichalcogenide 1T-TaS₂ upon inhibition of the metal-insulator transition. *Physical Review B* **81**, 172503 (2010).
- 20 Lahoud, E., Meetei, O. N., Chaska, K. B., Kanigel, A. & Trivedi, N. Emergence of a Novel Pseudogap Metallic State in a Disordered 2D Mott Insulator. *Physical review letters* **112**, 206402 (2014).
- 21 Cho, D., Cho, Y.-H., Cheong, S.-W., Kim, K.-S. & Yeom, H. W. Interplay of electron-electron and electron-phonon interactions in the low-temperature phase of 1T-TaS₂. *Physical Review B* **92**, 085132 (2015).
- 22 Ritschel, T. *et al.* Orbital textures and charge density waves in transition metal dichalcogenides. *Nature Physics* **11**, 328-331 (2015).
- 23 Darancet, P., Millis, A. J. & Marianetti, C. A. Three-dimensional metallic and two-dimensional insulating behavior in octahedral tantalum dichalcogenides. *Physical Review B* **90**, 045134 (2014).

- 24 Smith, N. V., Kevan, S. D. & DiSalvo, F. J. Band structures of the layer compounds 1T-TaS₂ and 2H-TaSe₂ in the presence of commensurate charge-density waves. *J. Phys. C: Solid State Phys* **18**, 3175 (1985).
- 25 Zwick, F. *et al.* Spectral Consequences of Broken Phase Coherence in 1T-TaS₂. *Physical review letters* **81**, 1058 (1998).
- 26 Clerc, F. *et al.* Lattice-distortion-enhanced electron-phonon coupling and Fermi surface nesting in 1T-TaS₂. *Physical Review B* **74**, 155114 (2006).
- 27 Marzari, N. & Vanderbilt, D. Maximally localized generalized Wannier functions for composite energy bands. *Physical Review B* **56**, 12847 (1997).
- 28 Souza, I., Marzari, N. & Vanderbilt, D. Maximally localized Wannier functions for entangled energy bands. *Physical Review B* **65**, 035109 (2001).
- 29 Mostofi, A. A. *et al.* wannier90: A Tool for Obtaining Maximally-Localised Wannier Functions. *Comput. Phys. Commun* **178**, 685 (2008).
- 30 Aryanpour, K., Pickett, W. E. & Scalettar, R. T. Dynamical mean-field study of the Mott transition in the half-filled Hubbard model on a triangular lattice. *Physical Review B* **74**, 085117 (2006).
- 31 Perfetti, L. *et al.* Time evolution of the electronic structure of 1T-TaS₂ through the insulator-metal transition. *Physical review letters* **97**, 067402 (2006).
- 32 Ma, L. *et al.* A metallic mosaic phase and the origin of Mott-insulating state in 1T-TaS₂. *Nature communications* **7**, 10956 (2016).
- 33 Cho, D. *et al.* Nanoscale manipulation of the Mott insulating state coupled to charge order in 1T-TaS₂. *Nature Communications* **7**, 10453 (2016).
- 34 Ye, C. *et al.* Visualizing the atomic-scale electronic structure of the Ca₂CuO₂Cl₂ Mott insulator. *Nature Communications* **4**, 1365 (2013).
- 35 Kresse, G. & Hafner, J. *Ab initio* molecular dynamics for liquid metals. *Phys. Rev. B* **47**, 558(R) (1993).
- 36 Kresse, G. & Hafner, J. *Ab initio* molecular-dynamics simulation of the liquid-metal-amorphous-semiconductor transition in germanium. *Phys. Rev. B* **49**, 14251 (1994).
- 37 Kresse, G. & Furthmüller, J. Efficiency of *ab-initio* total energy calculations for metals and semiconductors using a plane-wave basis set. *Comput. Mater. Sci* **6**, 15 (1996).
- 38 Kresse, G. & Furthmüller, J. Efficient iterative schemes for *ab initio* total-energy calculations using a plane-wave basis set. *Phys. Rev. B* **54**, 11169 (1996).
- 39 Kresse, G. & Joubert, D. From ultrasoft pseudopotentials to the projector augmented-wave method. *Phys. Rev. B* **59**, 1758 (1999).
- 40 Liechtenstein, A. I., Anisimov, V. I. & Zaanen, J. Density-functional theory and strong interactions: Orbital ordering in Mott-Hubbard insulators. *Physical Review B* **52**, R5467-R5470 (1995).

- 41 Dudarev, S. L., Botton, G. A., Savrasov, S. Y., Humphreys, C. J. & Sutton, A. P. Electron-energy-loss spectra and the structural stability of nickel oxide: An LSDA+U study. *Physical Review B* **57**, 1505 (1998).
- 42 Jellinek, F. The system tantalum-sulfur. *Less-Common Met.* **4**, 9 (1962).

Acknowledgements This work is supported by NSFC under grant No 11534007 and MOST under grant No 2015CB921000 of China. Z.L. is supported by Tsinghua University Initiative Scientific Research Program. H.Y. is supported by NSFC under Grant No. 11474175. Z.L. and H.Y. also acknowledge supports from the “Thousand Talents Plan of China” (for Young Professionals). N.W. and X.C. acknowledge the “Strategic Priority Research Program (B)” of the Chinese Academy of Sciences (Grant No. XDB04040100).

Author contributions Z.L., Y.W., J.W., and H.Y. conceived the project. N.W. and X.C. grew the 1T-TaS_{2-x}Se_x single crystals and performed transport measurements. X.L., W.R., C.Y., P.C. and Z.H carried out the STM measurements. S.Q., J.W., and Z.L. performed the DFT calculations. H.Y. and Z.L. contributed to the theoretical interpretations. S.Q., X.L., Y.W., and Z.L. prepared the manuscript.

Additional information Correspondence and requests for materials should be addressed to J.W., Y.W., and Z.L.

Competing financial interests The authors declare no competing financial interests.

Figures

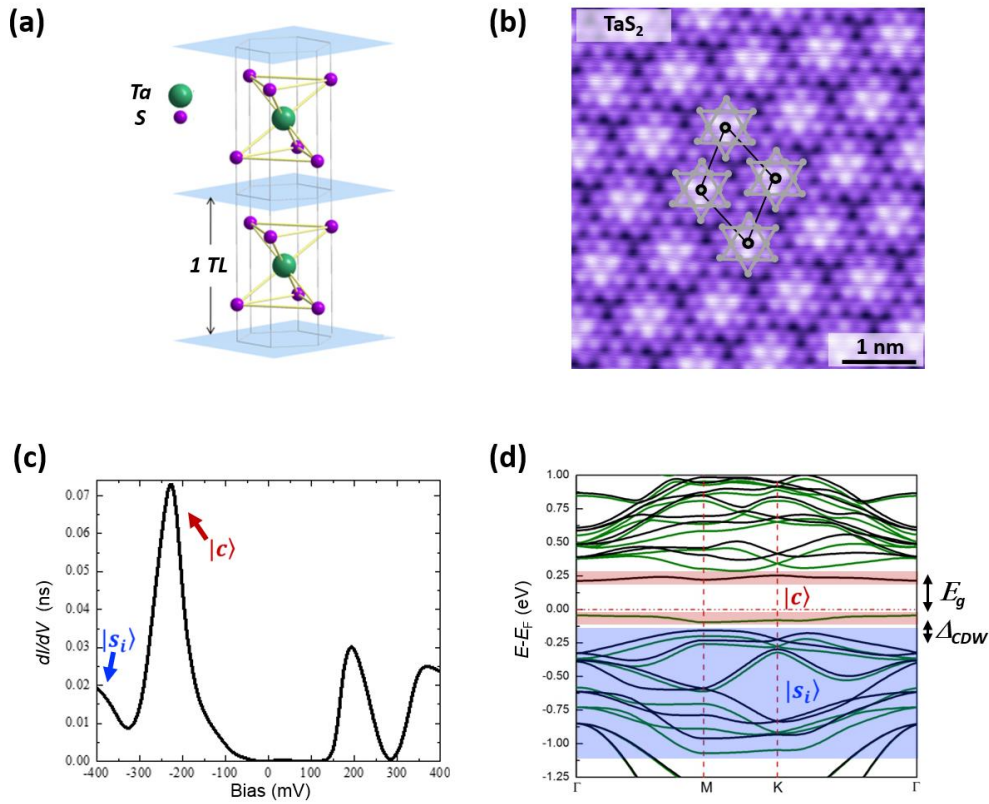


Figure 1 | Structural and electronic properties of 1T-TaS₂. a, Crystal structure of 1T-TaS₂. b, Atomic resolved topographic image of 1T-TaS₂ with bias voltage $V_b = 1$ V and tunneling current $I_t = 20$ pA. Each bright site on the surface corresponds to a S-atom in the topmost layer. The gray dots and the black lines mark the SD structure and the CCDW superlattice, respectively. The crystal cleaves easily between two adjacent S layers, as indicated by the blue planes in (a), exposing the triangular lattice of S atoms. c, Spatial averaged STM dI/dV spectrum acquired at 5 K. d, Fully relaxed DFT+U band structure of 1T-TaS₂. The two different colored curves represent the different spin components. The shaded regions indicate the energy range belonging to the different orbitals.

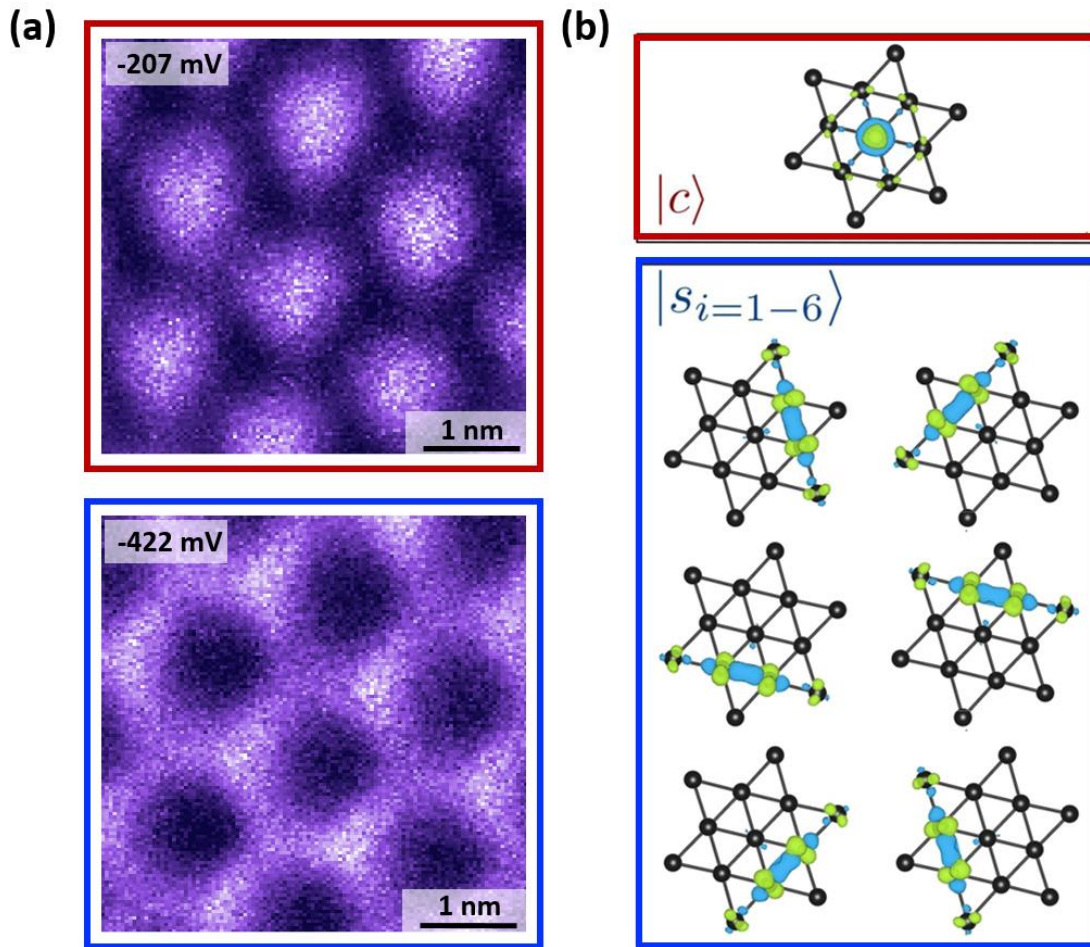


Figure 2 | Two types of orbital texture in $1T\text{-TaS}_2$. a, Differential conductance (dI/dV) maps ($42 \times 42 \text{ \AA}^2$) measured at $V_b = -0.2 \text{ V}$ (up) and $V_b = -0.4 \text{ V}$ (bottom) with tunneling current $I_t = 20 \text{ pA}$. The center of each CDW cluster is brighter at -0.2 V while the edges brighter at -0.4 V . b, Isovalue surface of two types of *ab initio* Wannier function.

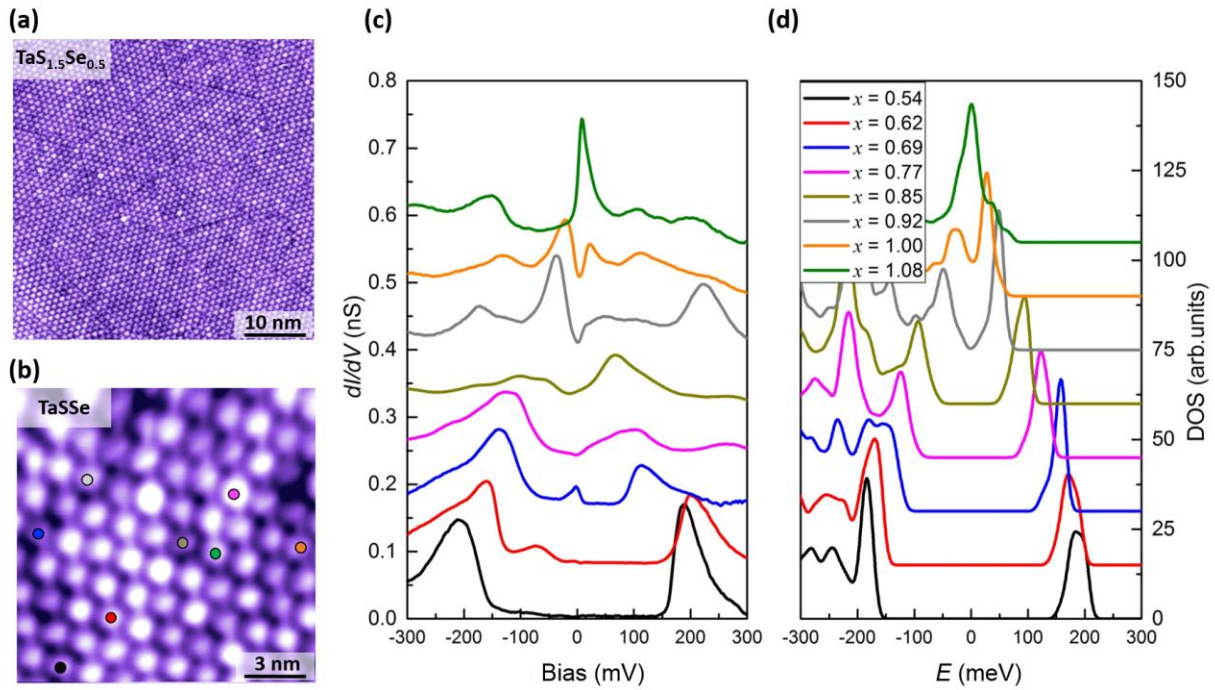


Figure 3 | Electronic structure evolution of Se substituted 1T-TaS_{2-x}Se_x. a,b, Topographic images of 1T-TaS_{2-x}Se_x with the averaged Se concentration $x = 0.5$ ($600 \times 600 \text{ \AA}^2$) and $x = 1$ ($130 \times 130 \text{ \AA}^2$), respectively. Each bright spots represent one CDW cluster and inhomogeneous intensity indicating the inhomogeneous doping level of different cluster. The large scale map of (a) shows clear domain feature and domain wall. c, Local STM dI/dV spectroscopy measured at various locations on the surface as marked in (b). d, DFT+U density of states of various Se concentration.

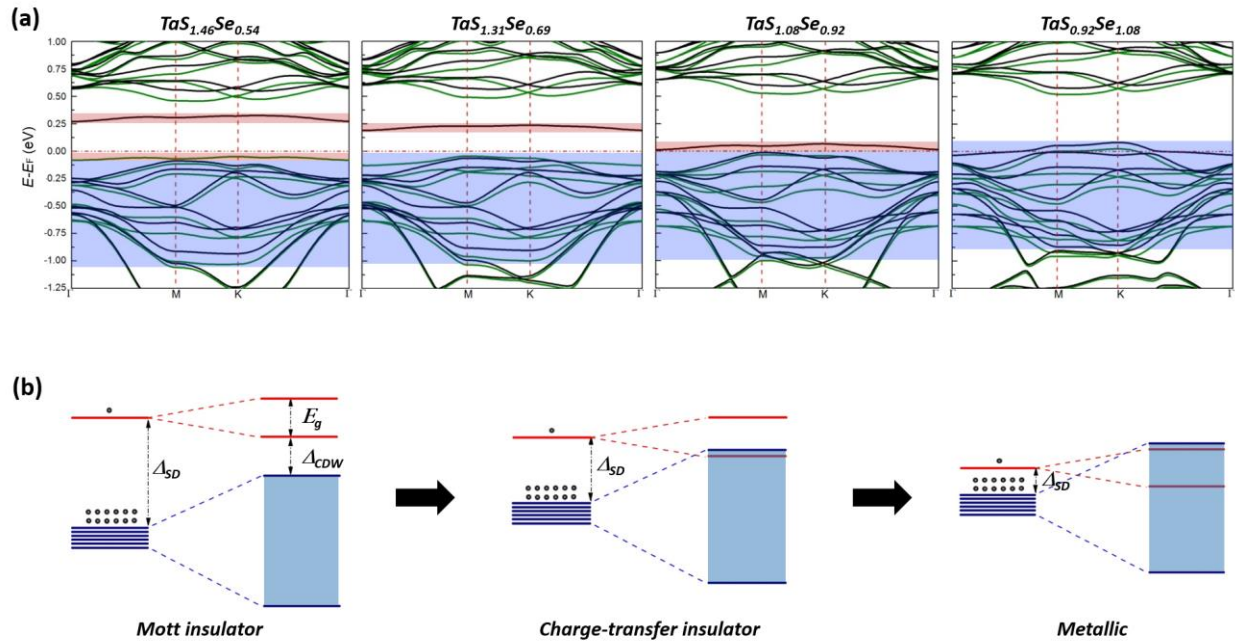


Figure 4 | DFT band structure and schematic energy diagram of 1T-TaS_{2-x}Se_x. a, Se substituted 1T-TaS_{2-x}Se_x results. The two different colored curves represent the different spin components. The shaded regions indicate the energy range belonging to the different orbitals. b, Energy level diagram of the Mott insulating phase, the charge-transfer insulator phase and the metallic phase.

Supplementary information for

**Orbital-driven Mottness collapse in 1T-TaS_{2-x}Se_x transition metal
dichalcogenide**

Shuang Qiao^{1,2,*}, Xintong Li^{1,*}, Naizhou Wang³, Wei Ruan¹, Cun Ye¹, Peng Cai¹, Zhenqi Hao¹,
Hong Yao^{2,4}, Xianhui Chen^{3,5}, Jian Wu^{1,4,†}, Yayu Wang^{1,4,†}, Zheng Liu^{2,4,†}

¹*State Key Laboratory of Low Dimensional Quantum Physics, Department of Physics, Tsinghua University, Beijing 100084, P.R. China*

²*Institute for Advanced Studies, Tsinghua University, Beijing 100084, P.R. China*

³*Hefei National Laboratory for Physical Science at Microscale and Department of Physics, University of Science and Technology of China, Hefei, Anhui 230026, P.R. China*

⁴*Innovation Center of Quantum Matter, Beijing 100084, P.R. China*

⁵*Collaborative Innovation Center of Advanced Microstructures, Nanjing University, Nanjing 210093, China*

*These authors contributed equally to this work.

†Email: wu@phys.tsinghua.edu.cn; yayuwang@tsinghua.edu.cn; zliu@phys.tsinghua.edu.cn

Contents:

- 1. Methods**
- 2. Supplementary experimental results**
- 3. Theoretical Wannier function analysis**

1. Methods

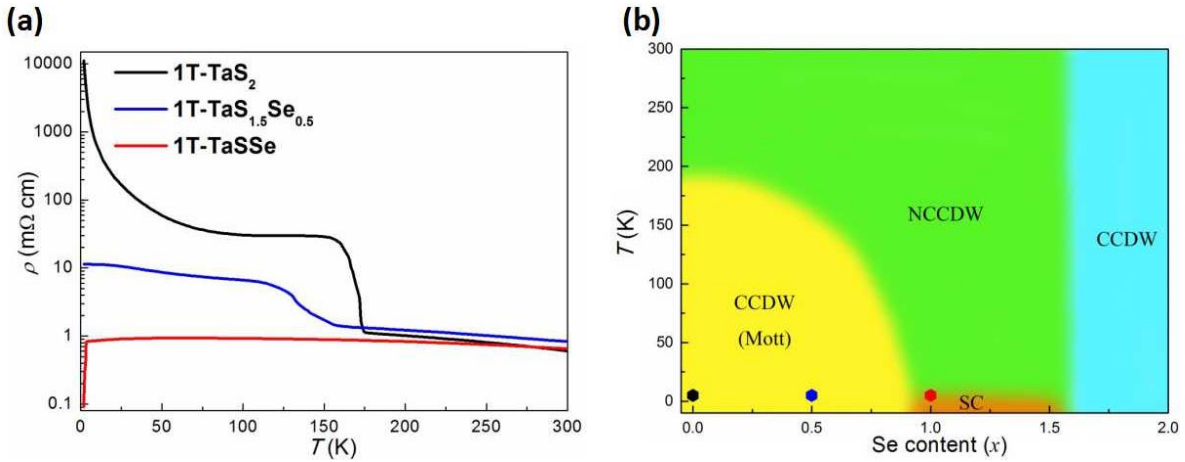
Crystal growth. The high-quality single crystals of $1T\text{-TaS}_{2-x}\text{Se}_x$ ($0 < x < 2$) were synthesized by chemical vapor transport method with iodine as transport agent. The powder of Ta, S, and Se is weighted stoichiometrically and thoroughly grounded. Then the mixture together with 150 mg I_2 is sealed into an evacuated quartz tube and then placed into a two-zone furnace with the temperature gradient of 1253 K-1153 K for 1 week. The products were washed with ethanol to remove the iodine at the surface.

STM and STS measurements. The STM experiments are performed with a cryogenic variable temperature ultrahigh vacuum STM system. The $1T\text{-TaS}_{2-x}\text{Se}_x$ crystal is cleaved in situ at $T = 77$ K and the measurement taken at 5 K with an electrochemically etched tungsten tip calibrated on a clean Au (111) surface³⁴. The STM topography is taken in the constant current mode, and the dI/dV spectra are obtained with a standard lock-in technique with modulation frequency $f = 423$ Hz.

DFT calculations. The first-principles calculation based on the density functional theory is performed using the Vienna *Ab-initio* Simulation Package³⁵⁻³⁸⁸ with a 280 eV plane-wave basis cutoff. The Perdew-Burke-Ernzerh generalized gradient approximation³⁹ and the projector augmented wave method³⁹ are employed. The $+U$ correction follows the simplified (rotational invariant) approach introduced by Dudarev^{40,41}. The integration over the Brillouin zone of the $\sqrt{13} \times \sqrt{13}$ supercell including 15 Å vacuum space is obtained on a Gamma-centered $6 \times 6 \times 1$ k mesh. The self-consistent iterations are converged to 10^{-5} eV precision of the total energy. We use the lattice parameters determined by experiment⁴², and relax the atomic coordination self-consistently until the forces are less than 0.002 eV/Å.

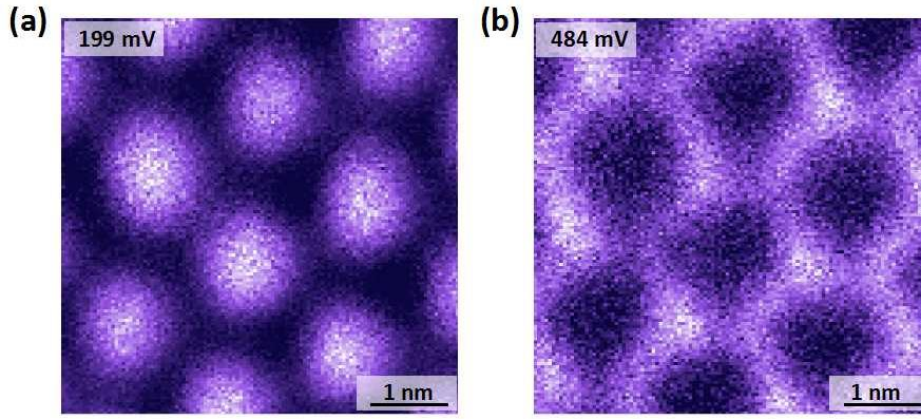
2. Supplementary experimental results

Figure S1a shows the in-plane resistivity data of three typical 1T-TaS_{2-x}Se_x samples. For the pristine 1T-TaS₂, there is a well-defined phase transition around 180 K, known to be the NCCDW-to-CCDW transition. Se substitution in the high-temperature NCCDW phase has little influence on transport, indicating that Se atoms are weak scatterers. However, Se substitution strongly suppresses the phase transition, and the discrepancy of the three samples in the low-temperature region becomes significant. A clear insulating behavior, which is commonly attributed to Mott localization, is found in the $x = 0$ sample below ~ 60 K. In contrast, the $x = 1$ sample keeps metallic until a sudden drop of resistivity ~ 3 K, which has been confirmed to be a superconducting transition. Figure S1b displays the location in the electronic phase diagram of these three 1T-TaS_{2-x}Se_x samples as derived from transport properties¹.



Supplementary Figure S1 | a, Temperature dependence of the in-plane resistivity. b, Schematic electronic phase diagram of 1T-TaS_{2-x}Se_x derived from transport properties as a function of temperature and x , the 3 points correspond to the same color line in (a).

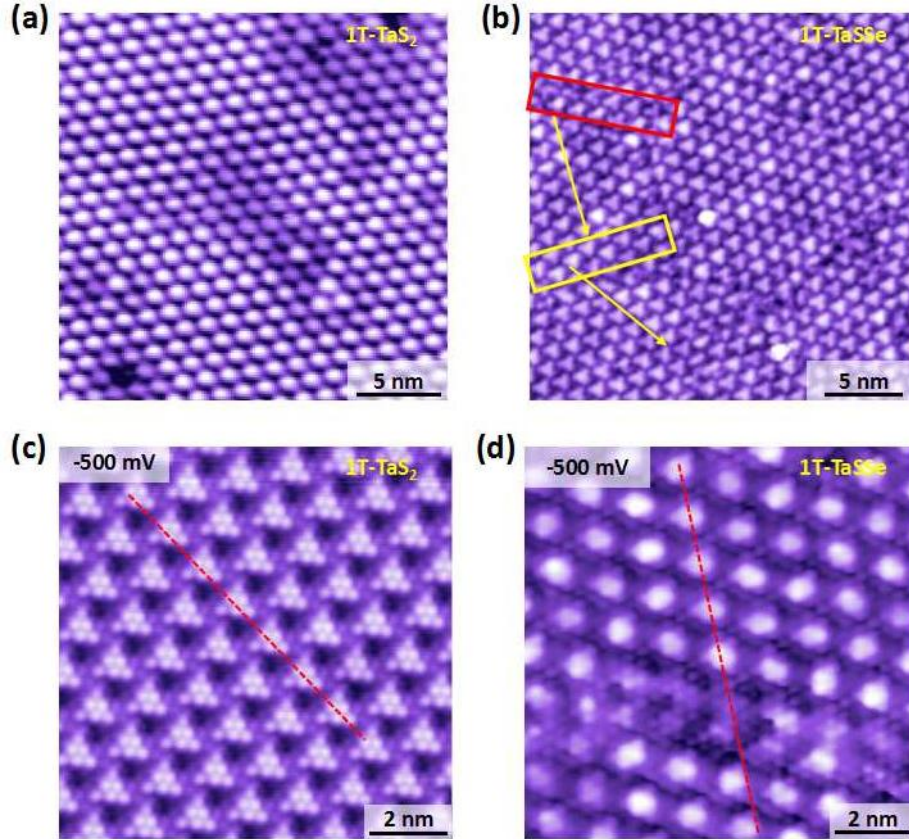
Figure S2 shows LDOS maps of the two representative energies measured at positive biases, exhibiting a periodic pattern commensurate with the SD superlattice. At the upper Hubbard band energy $V_b = 199$ mV (left panel), the bright spots locate in the center of SDs. While moving to higher energy with bias $V_b = 484$ mV (right panel), the bright regions shift to the surrounding Ta orbitals. These results are nearly symmetric with the maps at negative biases, demonstrating two types of orbital texture.



Supplementary Figure S2 | Differential conductance (dI/dV) maps ($42 \times 42 \text{ \AA}^2$) measured at $V_b = 199$ mV (left) and $V_b = 484$ mV (right) with tunneling current $I_t = 20$ pA. The center of each CDW cluster is brighter at 0.2 V while the edges brighter at 0.4 V.

Figure S3 displays a closer examination around the domain walls. Figure S3a,b are large scaled topographic images of 1T-TaS₂ and 1T-TaSe samples, respectively, in which each bright spot represent one CDW cluster. The uniform surface of parent compound is split into many domains in doped sample by domain boundary (red square). There is rotation between different domains as displayed by yellow arrows. Figure S3c,d are zoomed-in topographic images of Fig. S3a,b with atomic resolution. Red dashed lines indicate the super-lattice direction in both maps,

and half-cluster translation mismatch around domain boundaries is clearly demonstrated in Fig. S3d.



Supplementary Figure S3 | a,b, Large scaled topographic images of 1T-TaS₂ (225 × 225 Å²) and 1T-TaS₂Se (245 × 245 Å²) samples, each bright spot represent one CDW cluster. c,d, Zoom in topographic images of (a) and (b) with atomic resolution.

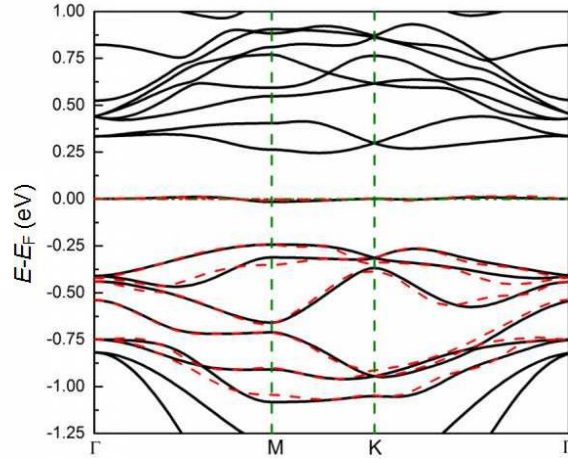
3. Theoretical Wannier function analysis

Figure S4 shows the first-principles band structure of a 1T-TaS₂ monolayer in the CCDW structure obtained within the framework of the generalized gradient approximation (GGA)² without spin degree of freedom. The most remarkable feature is a narrow band right at the Fermi

level. Besides, a set of 6 dispersive bands can be clearly differentiated below the Fermi level. These 6 bands along with the narrow band at the Fermi level consist of the downfolded seven-orbital subspace as we proposed in main text. We then perform Fourier transformation from the Bloch representation to the Wannier representation by using the WANNIER90 code³⁻⁵ within this subspace. The onsite energy and hopping parameters between these Wannier functions can be simultaneously calculated by performing the same Fourier transformation to the band eigenvalues. As shown in main text Fig. 2(b), the seven Wannier functions automatically separate into two groups, $|c\rangle$ and $|s_{\alpha=1\dots6}\rangle$. With respect to the onsite energy, $|s_{\alpha=1\dots6}\rangle$ are degenerate, as expected from symmetry; $|c\rangle$ is 0.21 eV higher. The largest hopping amplitude is between $|c\rangle$ and $|s_{\alpha=1\dots6}\rangle$, followed by several hopping processes among $|s_{\alpha=1\dots6}\rangle$. There is also considerable intercluster hopping for $|s_{\alpha=1\dots6}\rangle$. We list the leading matrix elements in Tab. SI. The set of obtained parameters for pristine 1T-TaS₂ is susceptible to a Mott transition owing to a large positive Δ_{SD} , which on the one hand separates $|s_{\alpha=1\dots6}\rangle$ far from the Fermi level, and on the other hand results in a small effective hopping between $|c\rangle$ of the order $O(t_{sc}^2 t_{ss} / \Delta_{SD}^2) \ll U$.

As the demonstration of the two-orbital-driven electronic transition, we manually increase the buckling of the S atoms around the central Ta by 0.187 Å and perform the same calculation and analysis. The results signal an insulator-to-metal transition tendency and a decrease of Δ_{SD} , rationalizing the concept of orbital-driven transition. Moreover, it is worth noting several points that bridges the structural and chemical modification. Firstly, the DFT structural relaxation shows that the substitutional Se atoms have nearly the same in-plane coordinates as S, but are about 0.187 Å above the S-plane. Meanwhile, the positions of Ta atoms hardly change. Therefore, Se substitution plays the effective role of increasing the local buckling of the trilayer. Secondly, the energy spectrum is found to be sensitive to the local buckling rather than the S/Se type. Using the

same buckled structure, very similar band structure can be obtained when replacing Se back to S. Finally, the similarity between structural and chemical modification is also reflected by comparing the extracted model parameters as shown in Tab. SI. In conclusion, structural modification and Se doping can be viewed as alternative ways to modulate the interplay between orbital textures, also manifesting the scenario of orbital-driven electronic transition.



Supplementary Figure 4 | DFT band structure of the 1T-TaS₂ monolayer without spin degree of freedom. The red dashed curves are the band structures by using the Wannier function basis.

TABLE SI:

Unit (eV)	Intrinsic	Deformed	Se-doped
Δ	0.212	0.143	0.146
t_{sc}	0.162	0.105	0.099
t_{ss1}	0.150	0.171	0.175
t'_{ss2}	0.091	0.087	0.089
t_{ss3}	0.072	0.013	0.021
t'_{ss4}	0.050	0.043	0.047
t_{ss5}	0.042	0.036	0.043

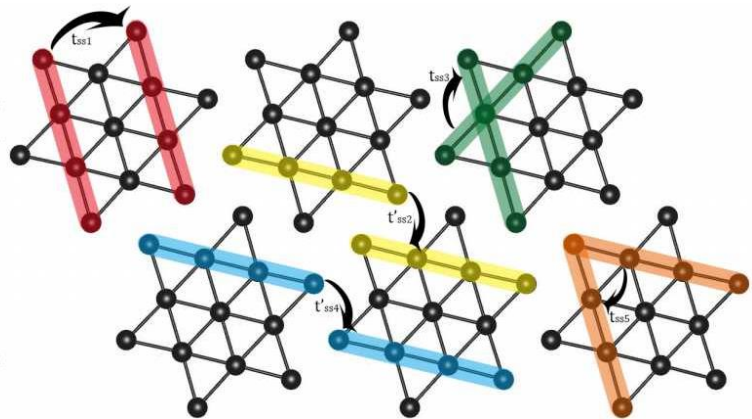


Table SI: Single-electron parameters from Wannier function analysis as used in Eq. (1) in the main context. The three columns correspond to the pristine 1T-TaS₂, an arbitrarily deformed 1T-

TaS₂ by manually increasing the out-of-plane distance between the central Ta and its nearest-neighbor S-atoms by 0.187 Å, and a Se-doped 1T-TaS_{2-x}Se_x with the Se concentration $x = 0.92$. The right figure shows the meaning of the five dominant hopping processes between the $|s_{i=1...6}\rangle$ -orbitals.

Supplementary References:

- 1 Liu, Y. et al. Superconductivity induced by Se-doping in layered charge-density-wave system 1T-TaS_{2-x}Se_x. *Appl. Phys. Lett.* **102**, 192602 (2013).
- 2 Perdew, J. P., Burke, K. & Ernzerhof, M. Generalized Gradient Approximation Made Simple. *Phys. Rev. Lett.* **77**, 3865 (1996).
- 3 Marzari, N. & Vanderbilt, D. Maximally localized generalized Wannier functions for composite energy bands. *Phys. Rev. B* **56**, 12847 (1997).
- 4 Souza, I., Marzari, N. & Vanderbilt, D. Maximally localized Wannier functions for entangled energy bands. *Phys. Rev. B* **65**, 035109 (2001).
- 5 Mostofi, A. A. et al. wannier90: A Tool for Obtaining Maximally-Localised Wannier Functions. *Comput. Phys. Commun* **178**, 685 (2008).